Chapter 4

Measurement of quasi elastic and transfer angular distribution of ^{10,11}B + ^{232}Th systems

4.1 Introduction

In heavy ion reactions, the interaction between the internal fabrication and the reaction dynamics of the colliding nuclei is very important at energies near the Coulomb barrier. It is a well know fact that the elastic scattering and transfer reactions are important for getting the information about different channel couplings. Since last many years, the study of elastic scattering angular distribution were carried out for various reactions with different optical model parameters. One of the important information from the study of heavy ion elastic scattering angular distribution around the Coulomb barrier is an unique behavior of potential parameters, and this is known as the threshold anomaly [1, 13]. This features can be understandable from the study of dispersion relation between the real and imaginary optical potential parameters [1, 13, 18].

The phenomena of threshold anomaly have been studied broadly in different heavy ion reactions with weakly/tightly bound projectiles. [2, 5, 13, 14, 15, 16, 17, 30, 31, 32, 33, 57]. The breakup threshold anomaly has been examined in weakly bound projectiles [3, 21, 25] because the breakup threshold energy of weakly bound projectile is less than tightly bound projectiles, as for example ^{6}Li (1.48 MeV), ^{7}Li (2.47 MeV),^{9}Be(1.57 MeV)

are less than ^{10}B(4.46 MeV) and ^{11}B (8.66 MeV). It is also observed that the fusion imaginary potential parameter shows the existence of threshold anomaly in tightly bound reactions. However the imaginary potential parameters of direct channel shows existence of breakup threshold anomaly. The elastic scattering and transfer angular distribution study for tightly bound projectiles like ^{10,11}B on heavy mass target ^{232}Th were not reported earlier and have very limited available results with other heavy mass targets [2, 17]. The use of heavy mass target is important for the investigation of threshold and breakup threshold anomaly.

In the present work, we have measured the quasi-elastic scattering (elastic + inelastic) and transfer angular distributions for both ^{10,11}B + ^{232}Th systems at different bombarding energies close to the Coulomb barrier. The Coulomb barrier for both systems is approximately 54 MeV. We have selected the energy range from 10% below to 20% above the Coulomb barrier. The low lying excited states of ^{232}Th target (0.49 KeV and 162 keV) could not be separated from the elastic peak in the present experimental technique and these inelastic contributions were included in the angular distribution data. Moreover, the isotopes corresponding to projectile Z = 5 could not be separated because of high counts of the elastic particles and hence the neutron transfer channels are also included in the quasi-elastic cross section. The inclusion of the inelastic channels with the elastic cross section have negligible effect in the results of the optical model analysis [80, 81]. In this chapter we have compared the reaction cross section with the transfer cross section and it gives information about the reaction mechanism and the structural nature of collide nuclei. The transfer processes are also dominant at below the barrier energies and they are effective in fusion cross section [75, 76, 82, 83]. A typical two-dimensional ΔE and E_{res} (residual energy) spectrum that have been obtained for the ^{11}B + ^{232}Th system at E_{lab} = 61 MeV and $\theta_{lab} = 90^{\circ}$ as shown in Fig.4.1.

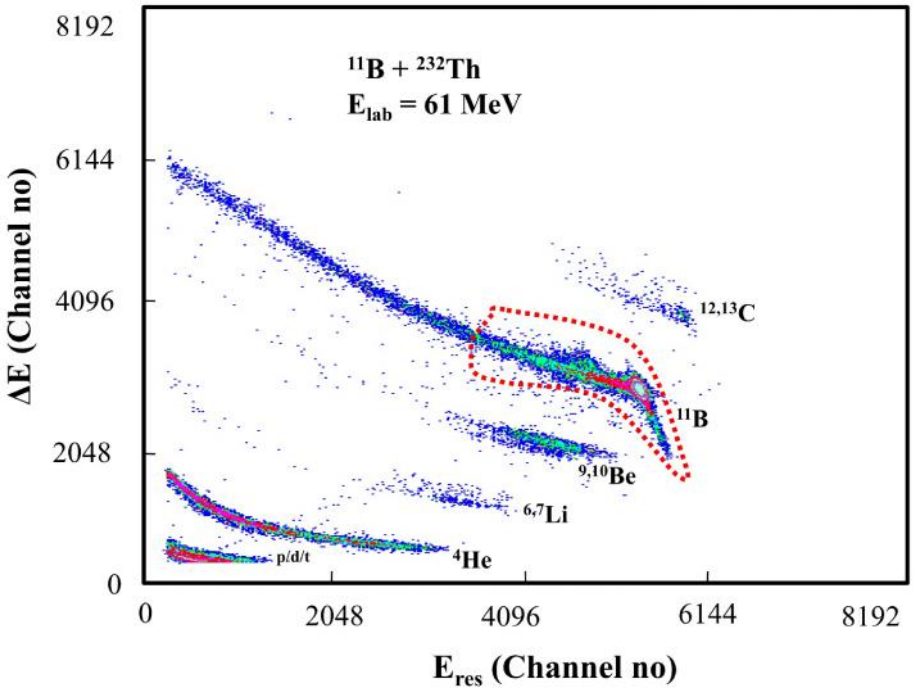

Figure 4.1: A typical two dimensional plot of ΔE versus E_{res} (residual energy) for the ^{11}B + ^{232}Th system at E_{lab} = 61 MeV and $\theta_{lab} = 90^o$. The bounded region (dashed line) on Z = 5 events shows quasi-elastic events.

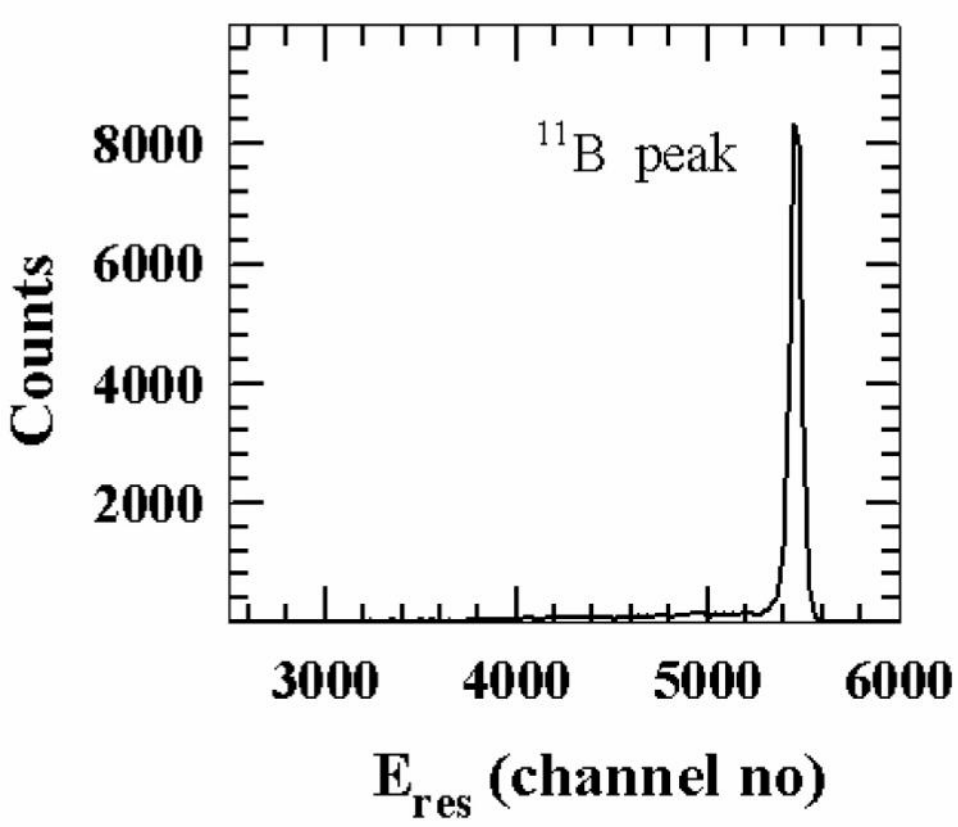

Figure 4.2: One dimension spectrum from above two dimensional figure (4.1) of the bounded region (dashed line) on Z = 5 events.

The dashed boundary in Fig.4.1 shows Z = 5 are quasi-elastic events and Fig.4.2 shows the 1D projection of the quasi-elastic peak which was used for the cross-section calculation. Since the low lying target excitation and also neutron transfer events could not be separated in the present experiment, therefore the angular distribution data will represent quasi-elastic cross section at all energies. LAMPS software has been used to perform all the experimental analysis. Details of the experiment and electronics setup have already been presented in chapter 2.

4.2 Data analysis

4.2.1 Optical model analysis of quasi elastic scattering and dispersion relation

In this work we have analyzed the quasi-elastic scattering angular distribution at different bombarding energies as shown in Figs. 4.3 and 4.4. The experimental quasi elastic scattering angular distribution data was analyzed by using Woods Saxon potential ECIS code (Equations Couplees en Iterations Sequentielles) [64]. For the study of elastic scattering, quasi elastic scattering, inelastic scattering, fusion excitation functions, and barrier distributions the optical potential have been successfully employed. In the beginning of fitting process of angular distribution, the radial optical potential parameters (real and imaginary) were permitted to vary with constant depths and diffuseness parameters.

We have obtained best the fitting optical potential parameters after the variation of radius, diffuseness and depth both real and imaginary parameters. The best fitted radius and diffuseness parameters were 1.06 fm 0.71 fm respectively for all energies. In the analysis procedure, radius and diffuseness parameters were kept fixed and only depth parameters was varied to obtain χ^2 minimization.

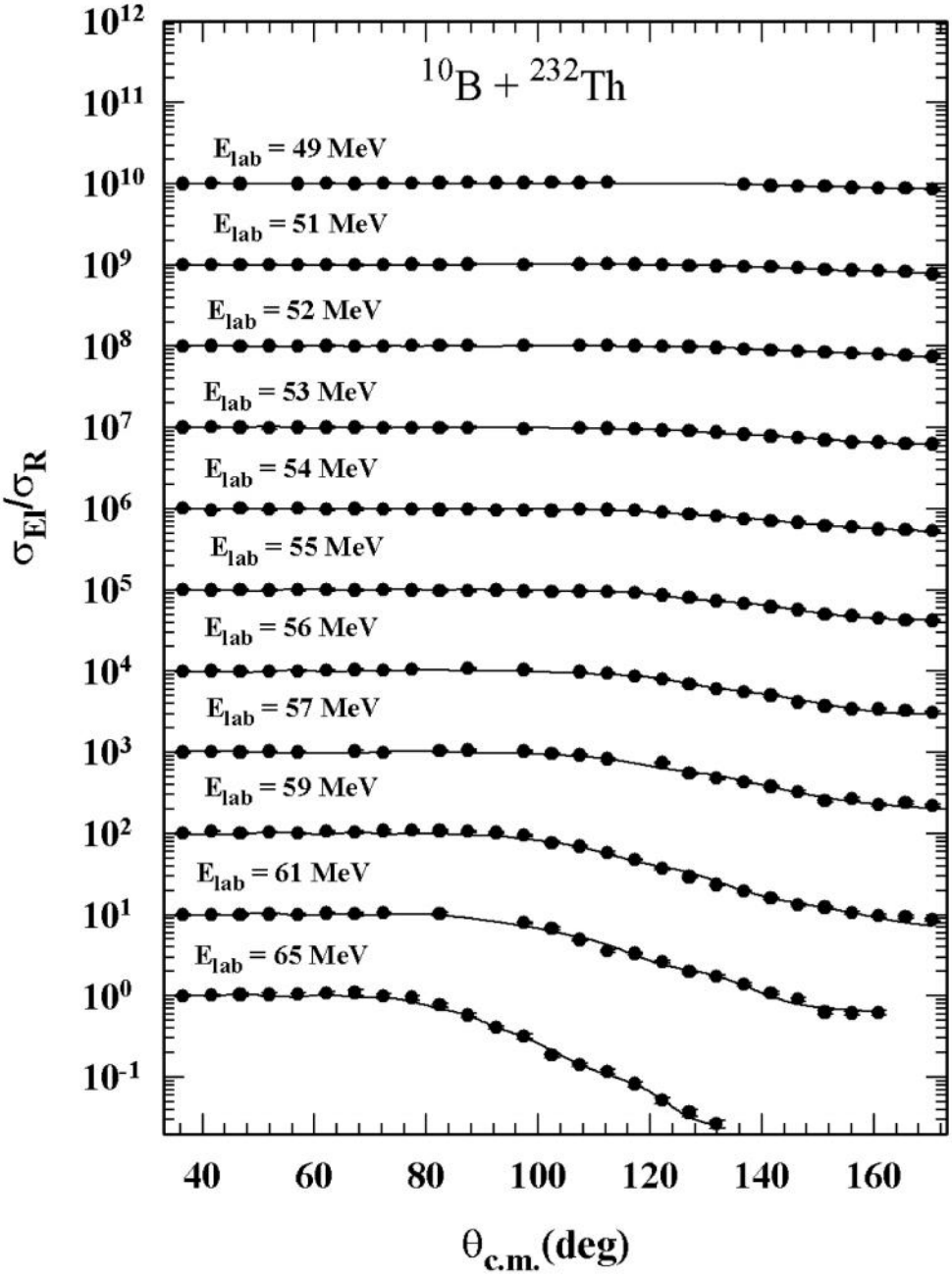

Figure 4.3: Quasi-elastic scattering angular distributions normalizes with Rutherford cross section for ^{10}B + ^{232}Th system at various energies after suitably scaling. Solid line represents Woods-Saxon fitting procedure.

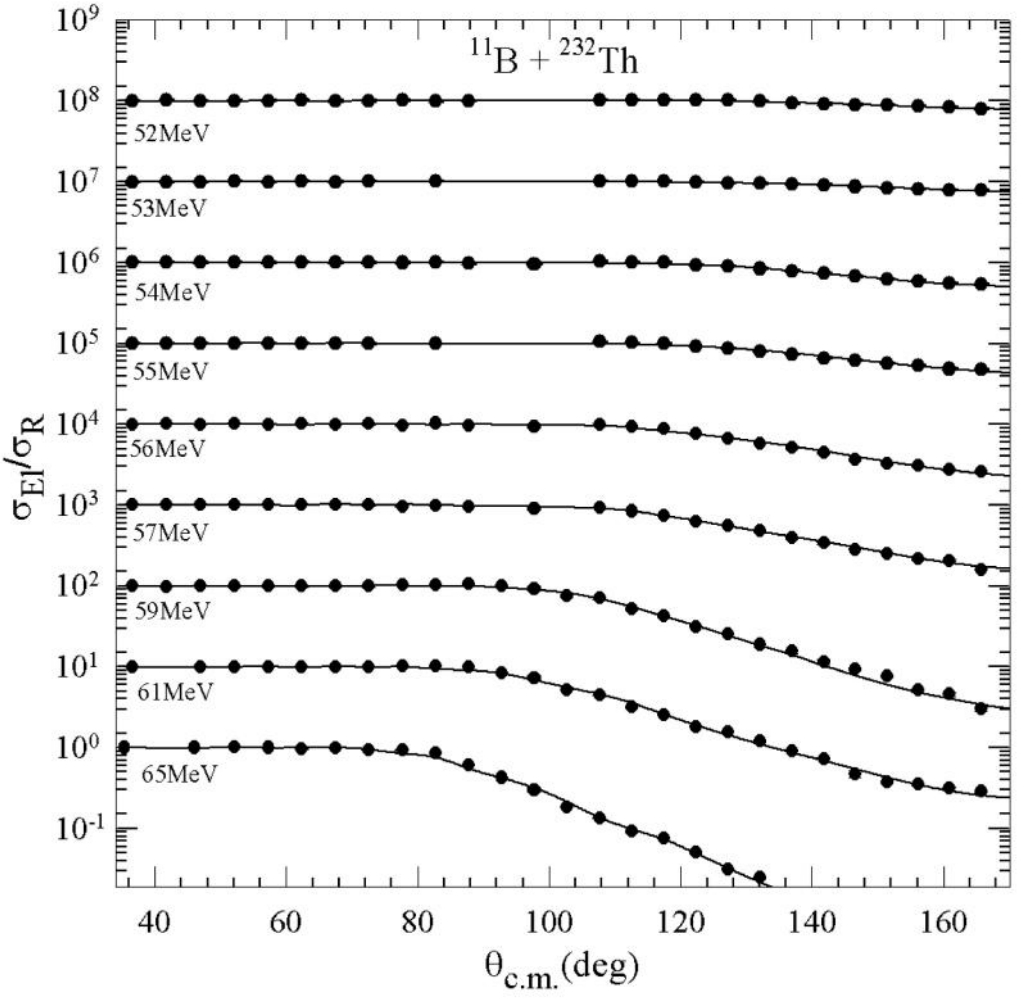

Figure 4.4: Quasi-elastic scattering angular distributions normalizes with Rutherford cross section for ^{11}B + ^{232}Th system at various energies after suitably scaling. Solid line represents Woods-Saxon fitting procedure.

The result of fitting procedure of the angular distributions are shown in Figs. 4.3 and Fig. 4.4 for ^{10,11}B + ^{232}Th systems respectively. Corresponding best fitted optical potential parameters for the optical model analysis are given in tables 4.1 and 4.2 for ^{10,11}B + ^{232}Th systems respectively [35]. We have obtained strong sensitivity of radius at each energies for both the systems. Figs. 4.5 and 4.6 represent the strong sensitive radius for ^{10,11}B + ^{232}Th systems respectively at 65 MeV. The center of intersection has been recognized as a radius of a sensitivity [27, 30, 31, 32, 57, 84]. For the analysis of sensitive radius we have fixed the radius parameters and varied the depth parameters for each of the diffuseness parameters from 0.67, 0.69, 0.71, 0.73 to 0.75 fm, for all the beam energies. The average sensitivity of radius for ^{10}B + ^{232}Th system is 12.39 fm and for ^{11}B + ^{232}Th system is 12.45 MeV [35]. Fig. 4.7 shows the relation of energy dependent real and imaginary optical potential parameters, these parameters were taken from tables 4.1 and 4.2 for ^{10,11}B + ^{232}Th reactions. The error bars included in the experimental data (Fig. 4.7) have been obtained from the divergence of the potential parameters corresponding to 1 unit changes in the χ^2 value. The procedure of dispersion relation analysis has been given in chapter 2 (section 2.9). The result of optical potential parameters shows threshold anomaly in both systems as shown in Fig. 4.7, which was detected earlier for ^{12}C, ^{16}O tightly bound nuclei [13, 30, 31]. Two different sets of the real optical potential parameters were extracted by numerical calculation of DR equation using two different line segment fits of imaginary part of potential W(E) [20].

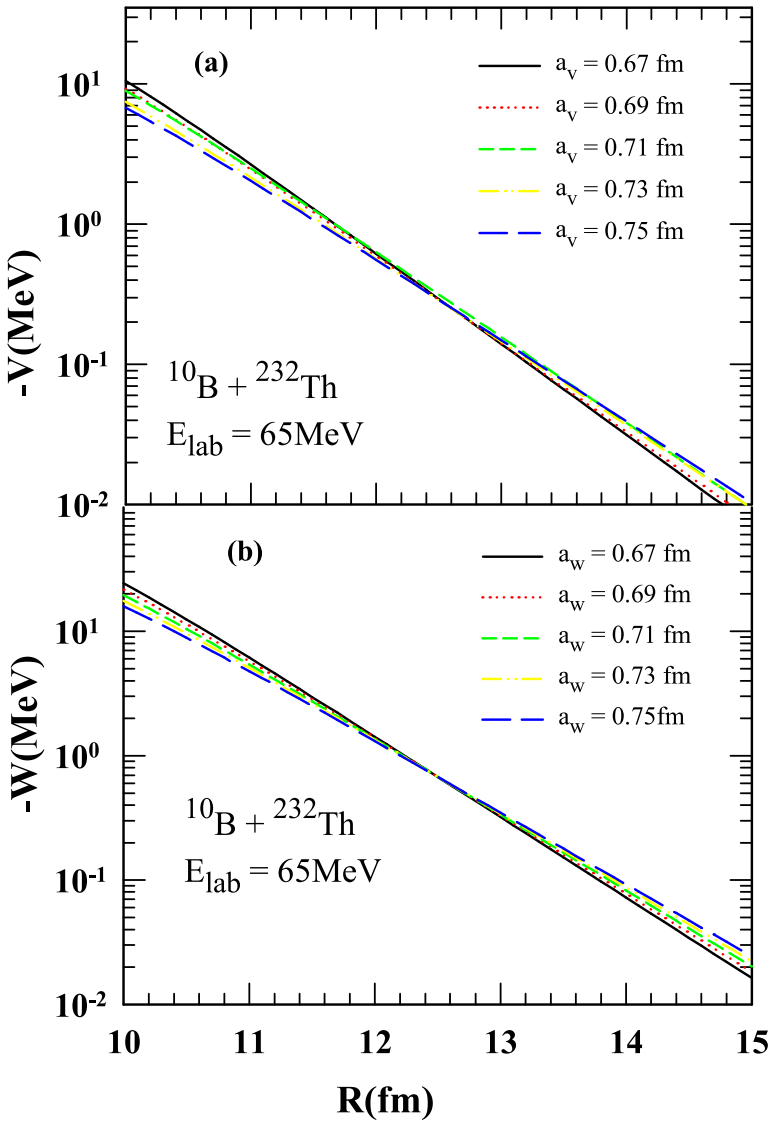

Figure 4.5: Sensitivity radii based on the crossing of the real (a) and imaginary (b) parts of the WSP potential at E_{lab} = 65 MeV for different diffuseness parameter values (a_v and a_w).

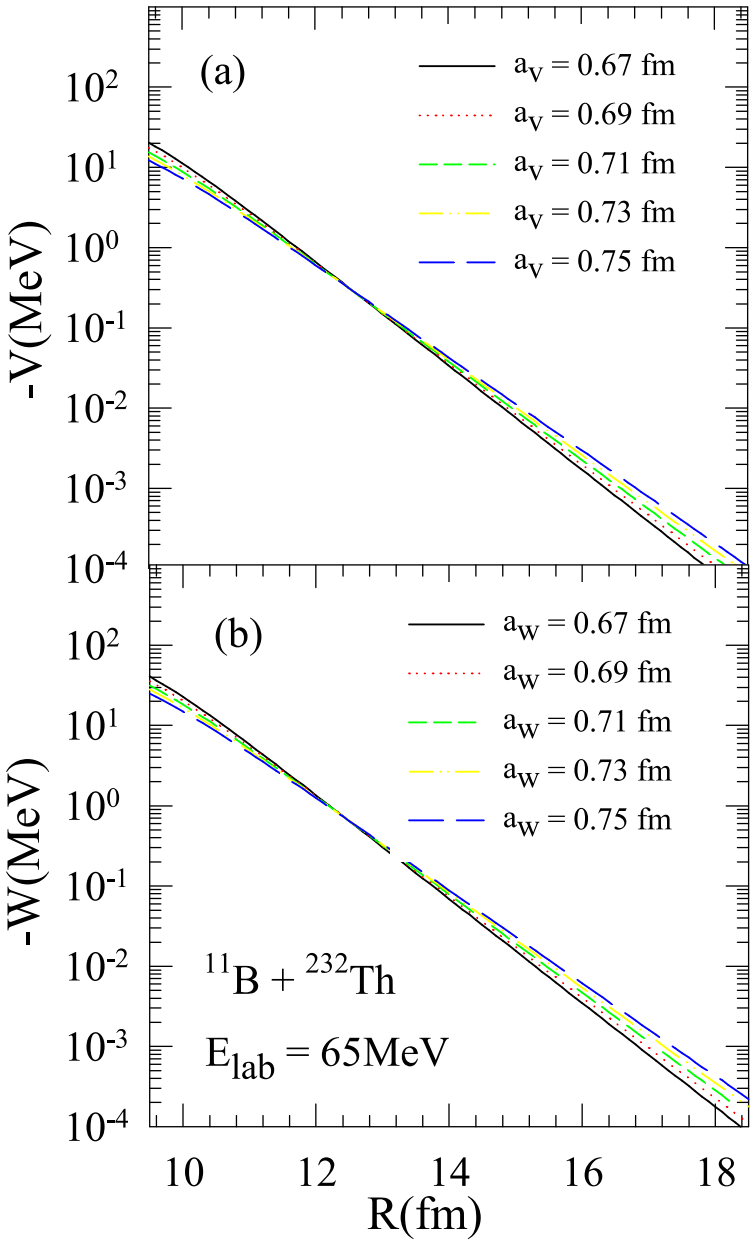

Figure 4.6: Sensitivity radii based on the crossing of the real (a) and imaginary (b) parts of the WSP potential at E_{lab} = 65 MeV for different diffuseness parameter values (a_v and a_w).

Table 4.1: Optical potential parameters and total reaction cross sections (σ_R) of ^{10}B + ^{232}Th system obtained using ECIS code. The transfer reaction cross sections (σ_{tr}) are also presented.

E_{lab}(MeV)	V_r(MeV)	V_i(MeV)	$\frac{\chi^2}{n}$	σ_R(mb)	σ_{tr}(mb)
49	492.4	6.49	0.87	6.24	2.23 ± 0.47
51	294.5	11.60	0.23	16.10	4.09 ± 0.68
52	218.2	18.63	0.26	38.73	6.06 ± 1.20
53	153.0	55.74	0.21	90.97	9.64 ±1.17
54	132.8	55.99	0.84	121.81	13.61 ± 1.42
55	128.4	50.90	0.55	153.52	16.55 ± 1.30
56	120.8	49.50	4.35	197.20	21.61 ± 1.22
57	106.4	57.23	3.48	264.91	30.18 ± 2.40
59	83.47	86.76	5.84	451.72	41.95 ± 1.66
61	59.07	84.00	3.76	551.22	48.89 ± 1.65
65	77.85	92.62	2.43	824.50	54.81 ± 4.49

Table 4.2: Optical model parameters [27] and transfer (σ_{tr}) as well as total reaction cross section (σ_R) values for ^{11}B + ^{232}Th system at different energies.

E_{lab}(MeV)	V_r(MeV)	V_i(MeV)	$\frac{\chi^2}{n}$	σ_R(mb)	σ_{tr}(mb)
52	194.0	0.13	1.58	7.02	6.21 ± 0.56
53	149.2	15.03	0.64	29.81	8.39 ± 0.53
54	162.0	31.43	1.21	89.74	14.44 ± 0.93
55	134.2	27.32	4.06	105.40	16.09 ± 1.01
56	126.0	51.44	3.52	216.21	24.77 ± 1.35
57	109.4	57.02	4.70	279.72	35.75 ± 1.15
59	121.5	59.23	4.90	432.61	37.80 ± 2.16
61	73.67	89.30	11.2	601.70	38.79 ± 1.47
65	53.45	109.70	9.21	886.42	42.27 ± 1.48

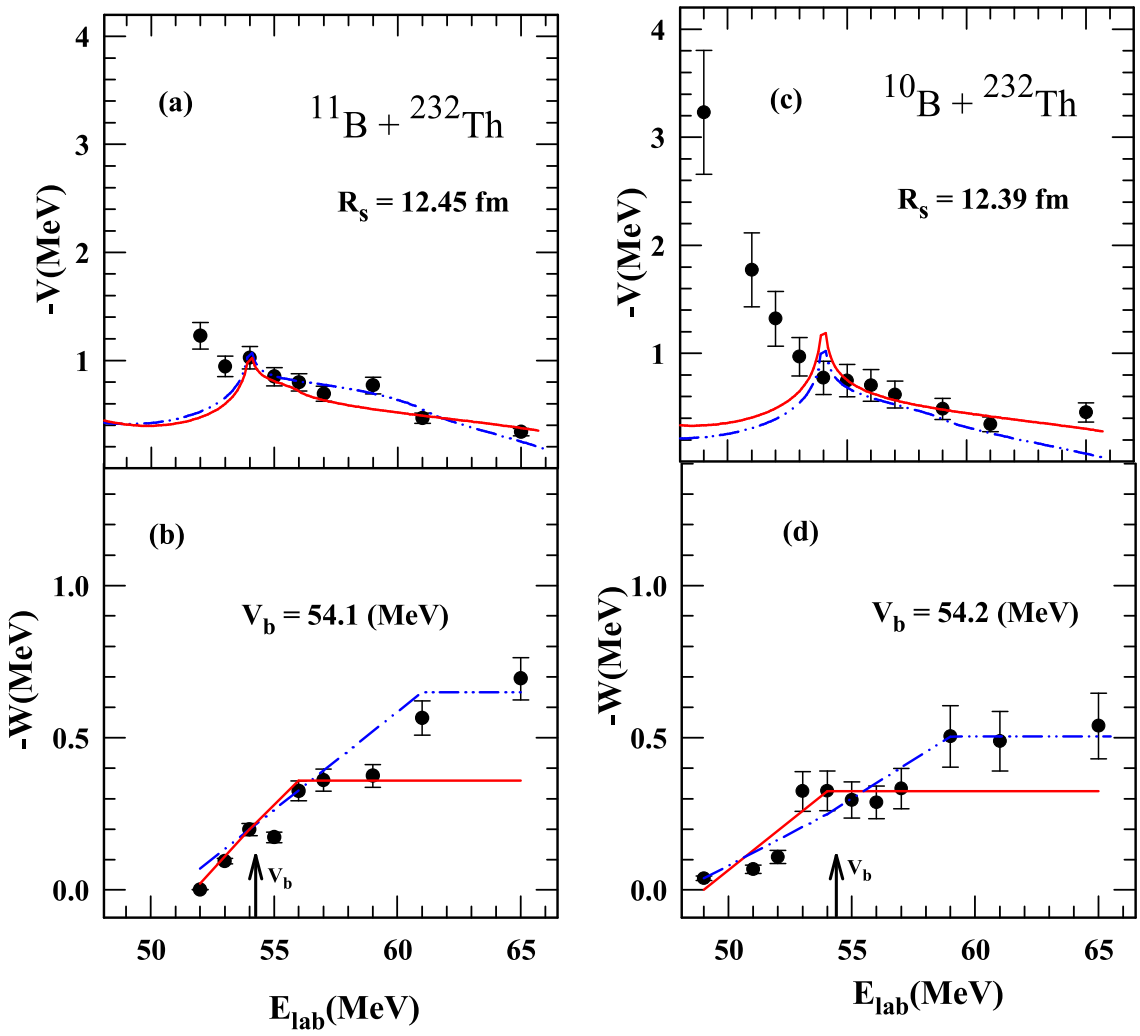

Figure 4.7: Energy dependence of the real and imaginary potentials at sensitivity radii R_s = 12.39 fm for ^{10}B + ^{232}Th system in Panels (a), (b) and at R_s = 12.45 fm for ^{11}B + ^{232}Th in panels (c), (d). Solid (red) and dashed (blue) lines are two different sets of line-segment fits. Arrows in the panels (b) and (d) indicate the positions of Coulomb barriers (V_b) for ^{11}B + ^{232}Th and ^{10}B + ^{232}Th, respectively.

4.2.2 Analysis of the transfer angular distribution

The experimental data for the angular distribution of the transfer products ^{12,13}C, ^{9,10}Be and ^{6,7}Li were analyzed at various angles. Same experimental setup were used for the measurement of transfer angular distribution as shown in Fig. 2.8 chapter 2. The transfer cross sections were obtained from the yield of the transfer products at various angles normalized with the Rutherford scattering events at forward angles. The transfer angular distribution is shown in Fig. 4.8 for ^{10,11}B + ^{232}Th reactions, at different projectile energies.

In the case of ^{2}H or ^{3}H transfer from ^{10,11}B respectively, the projectile-like fragment will be ^{8}Be and it will immediately break into two a particles [85, 34]. In this analysis, alpha particles are also not included as these are coming from compound nucleus evaporation [85]. The overall transfer data shows a bell-shaped angular distribution as shown in Fig. 4.8. The grazing angle corresponding to the maximum yield shifts towards back angle with the reduction of the beam energy. The transfer cross sections for each energies are presented in tables 4.1 and 4.2 for both ^{10,11}B + ^{232}Th reactions, respectively.

In this thesis work we have compared transfer cross section with the total reaction cross sections for both the systems as shown in Fig. 4.9. The transfer cross section of both systems show similar behavior but the total reaction cross section of ^{10}B + ^{232}Th system is larger than ^{11}B + ^{232}Th system at sub barrier energies.

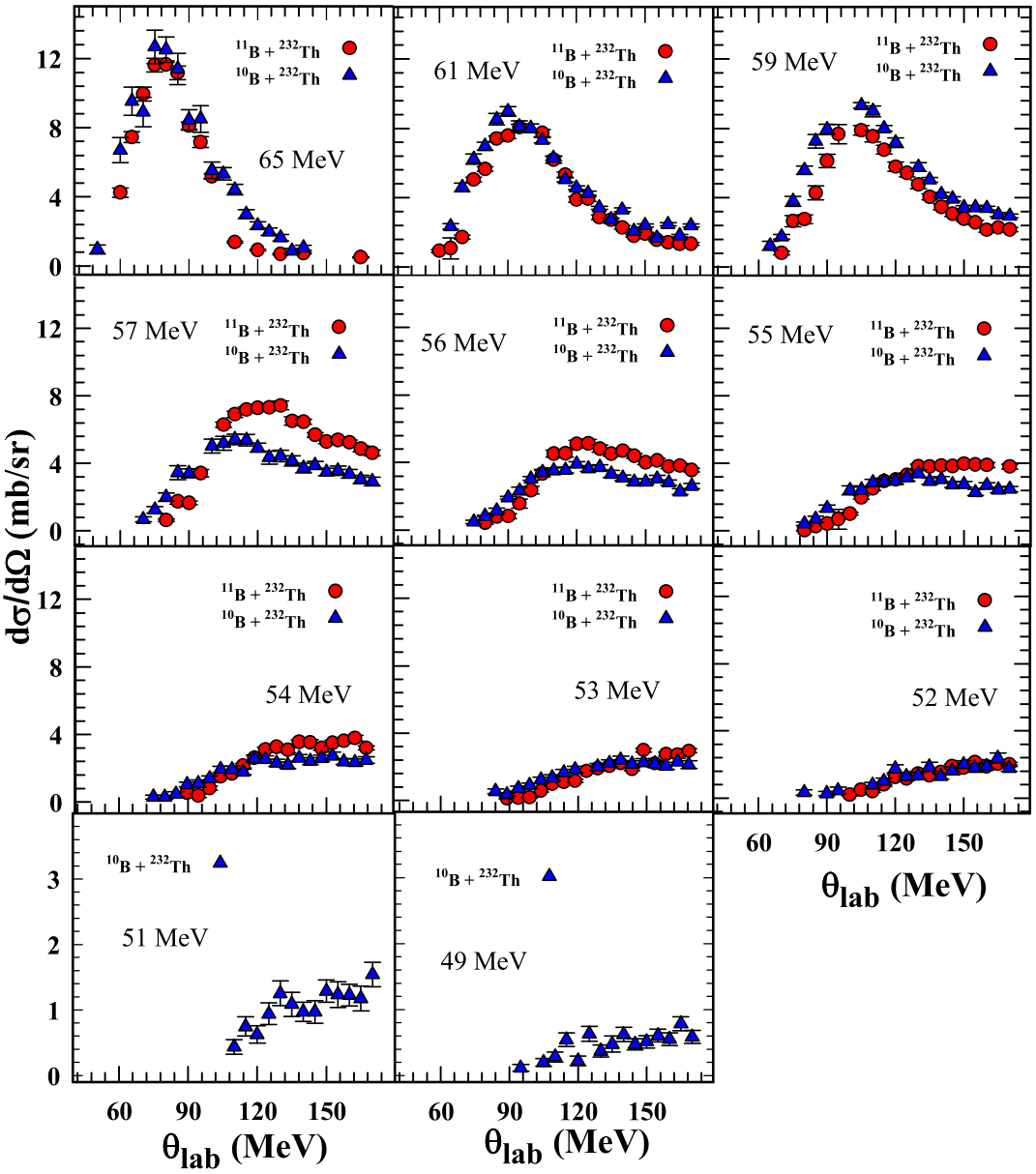

Figure 4.8: Transfer angular distributions for ^{12,13}C, ^{9,10}Be and ^{6,7}Li at various bombarding energies for ^{10,11}B + ^{232}Th systems.

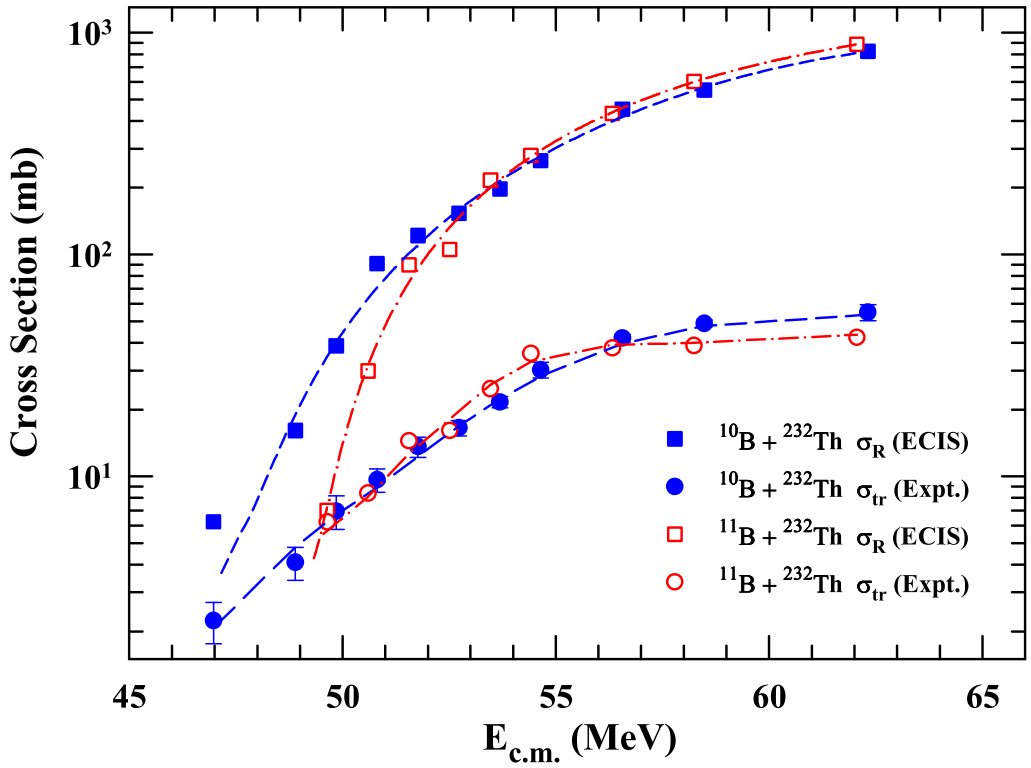

Figure 4.9: Total reaction cross sections for ^{10}B + ^{232}Th system (solid square) and ^{11}B + ^{232}Th system (open square) derived from fit to the quasi-elastic scattering angular distribution using the ECIS code. The transfer cross section (only sum of ^{12,13}C ^{9,10}Be and ^{6,7}Li) are plotted for ^{10}B + ^{232}Th (solid circles) and for ^{11}B + ^{232}Th (open circles). Dashed and dash-dotted lines are guide to eye.

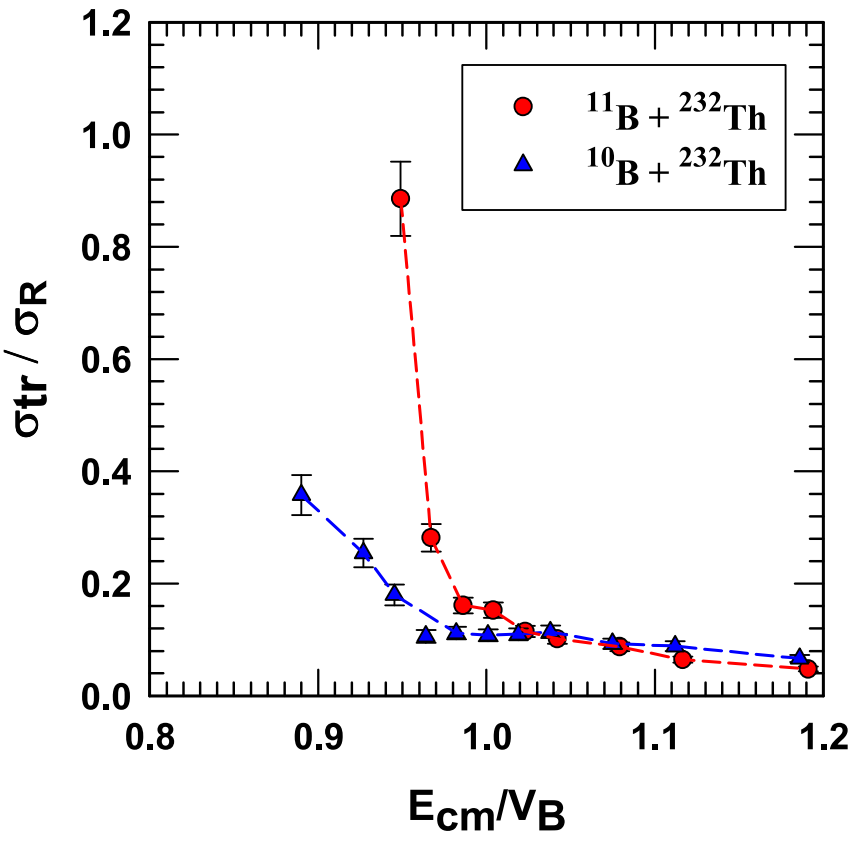

Figure 4.10: The fraction of the transfer cross section ($\sigma_{\rm tr}$) to the total reaction cross sections ($\sigma_{\rm R}$) as a function of the beam energies for the both ^{11,10}B + ^{232}Th systems. The dashed curves are guide to eye.

In Fig. 4.10, the ratio of the transfer cross section ($\sigma_{\rm tr}$) and the total reaction cross section ($\sigma_{\rm R}$) has been plotted as a function of the beam energy for both ^{10,11}B + ^{232}Th systems. It can be seen that at energies above the Coulomb barrier, this ratio shows a saturation and at sub-barrier energies it increases sharply for both the systems. The fraction of the transfer cross section in comparison to the total reaction cross section is significantly large for ^{11}B + ^{232}Th as compared to ^{10}B + ^{232}Th system at energies below the Coulomb barrier.

4.3 Reduced total reaction cross section calculation

In order to study the projectile effect for various reactions, it is required to compress disparities arising from the size and charges of the reactions [27]. The method of reduction introduced by Gomes *et al.* has been widely applied for this type of work to understand the reaction mechanism [77]. In this reduction method, the required quantities are total reaction cross section $\sigma_{\rm R}$, mass of the projectile $A_{\rm P}$ and target $A_{\rm T}$, energy in center of mass $E_{\rm c.m.}$, charge of the projectile $Z_{\rm P}$ and the target $Z_{\rm T}$. Fig. 4.11(a) represents the reduced reaction cross section graph for the four systems, where X axis is $E_{\rm c.m.}(A_{\rm P}^{1/3} + A_{\rm T}^{1/3})/\ Z_{\rm P}Z_{\rm T}$ and Y axis is $\sigma_{\rm R}/(A_{\rm P}^{1/3} + A_{\rm T}^{1/3})^2$. This method has been used in many previous studies [27, 29, 35, 78, 79, 84]. In the second method of reduced reaction cross section the X axis is $\rm E_{c.m.}/V_b$ and Y axis is $\sigma_{\rm R}/\pi {\rm R}_{\rm b}^2$, as shown in Fig. 4.11(b) [86]. The reduction method suggests that this mechanism recapture the dependence on the mass and charge of the colliding nuclei, but this mechanism does not have the character of projectile density, especially for weakly bound projectiles [27]. The comparison of the reduced reaction cross sections of four systems, ^{6,7}Li + ^{232}Th and ^{10,11}B + ^{232}Th are shown in Fig. 4.11. It was observed that the total reaction cross section for ^{10,11}B + ^{232}Th systems (^{11}B + ^{232}Th data is from [35]) are smaller than the ^{6,7}Li + ^{232}Th systems [29].

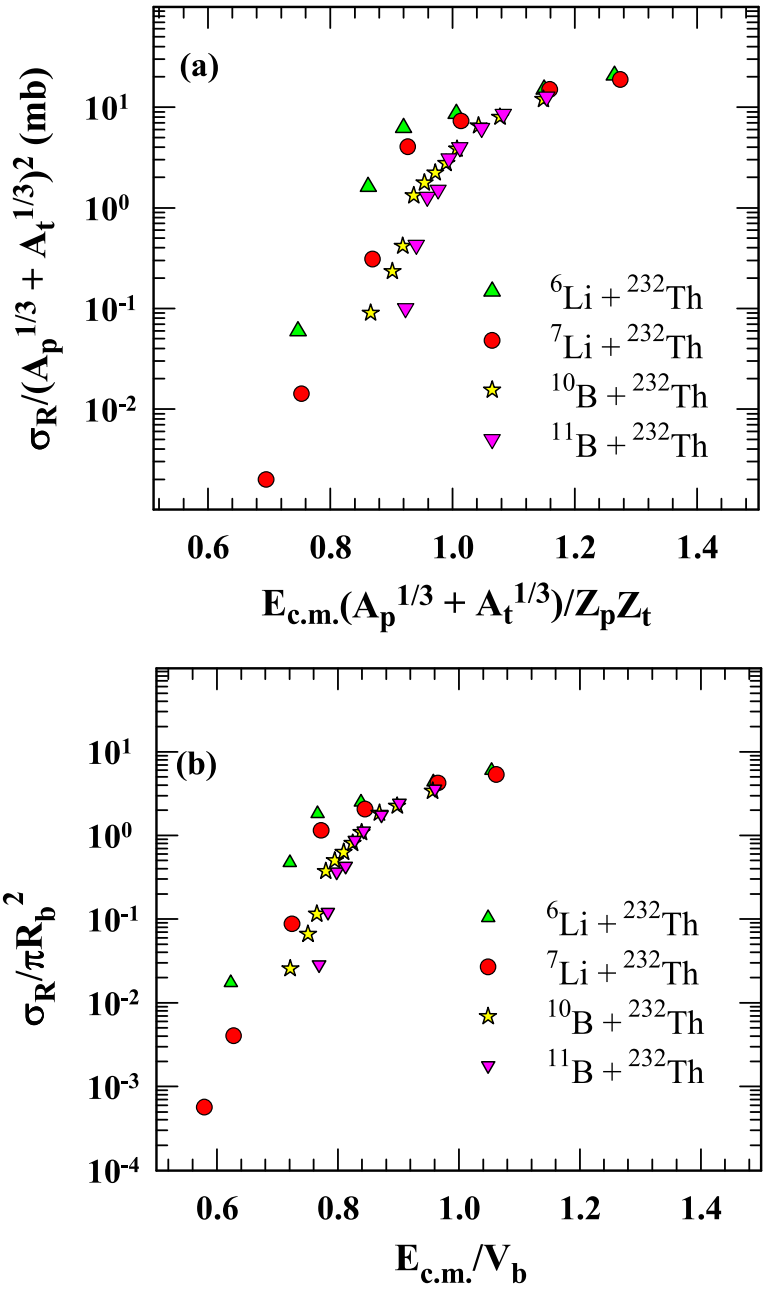

Figure 4.11: Reduced total reaction cross section for the ^{10,11}B + ^{232}Th systems compared with ^{6,7}Li + ^{232}Th systems [26] using the two reduction procedures (first taken from reff [26,67,78] and second taken from [78] as mention in the text).

4.4 Results and Discussion

In this work we have measured the quasi-elastic scattering and transfer angular distribution for the ^{10,11}B projectiles on ^{232}Th target at different energies close to the Coulomb barrier. The experimental results were analyzed in the terms of the optical mode by using the Woods- Saxon potential. Using suitable fitting procedure between experimental and theoretical results, it was possible to obtain the real and imaginary parts of the optical potential. From this analysis, it was observed that the real optical potential parameters increases and corresponding imaginary optical potential parameter decreases for both systems. This type of behavior indicates the presence of threshold anomaly (TA) in both ^{10,11}B + ^{232}Th systems. The transfer and total reaction cross sections were also obtained for both systems.